

## Baffled fuel-storage container: parametric study on transient dynamic characteristics

Sang-Young Lee<sup>†</sup> and Jin-Rae Cho<sup>‡</sup>

*School of Mechanical Engineering, Pusan National University, Pusan 609-735, Korea*

Tae-Hak Park<sup>‡†</sup> and Woo-Yong Lee<sup>‡‡</sup>

*Agency for Defense Development, Daejeon 305-600, Korea*

*(Received June 13, 2001, Accepted January 21, 2002)*

**Abstract.** In order to ensure the structural dynamic stability of moving liquid-storage containers, the flow motion of interior liquid should be appropriately suppressed by means of mechanical devices such as the disc-type elastic baffle. In practice, the design of a suitable baffle requires *a priori* the parametric dynamic characteristics of storage containers, with respect to the design parameters of baffle, such as the installation location and inner-hole size, the baffle number, and so on. In this paper, we intend to investigate the parametric effect of the baffle parameters on the transient dynamic behavior of a cylindrical fuel-storage tank in an abrupt vertical acceleration motion. For this goal, we employ the ALE (arbitrary Lagrangian-Eulerian) kinematic description method incorporated with the finite element method.

**Key words:** baffled fuel-storage container; installation location and inner-hole size; transient dynamic characteristics; parametric numerical analysis; ALE method.

---

### 1. Introduction

The moving fuel-storage container is a considerable research subject in the fluid-structure interaction community. This is because not only the hydrodynamic force influences crucially the structural and maneuvering stability of vehicles, but also the interior fuel flow exhibits a variety of dynamic characteristics to the major design parameters. Naturally, the remarkable research efforts have focused, according to the development initiation of space vehicles in the period of 1950-1960, for the dynamic modeling and characteristic analysis of fuel-storage containers aiming at the stable and safe design of such vehicles. The early research studies are summarized in the works by Abramson *et al.* (1961 and 1964). In which, most of early theoretical and experimental research results for various tank models, together with the damping effects of various baffles, are well addressed. However, the early theoretical and numerical studies were quite restricted, owing to the insufficient

---

<sup>†</sup> Ph.D. Student

<sup>‡</sup> Associate Professor

<sup>‡†</sup> Principal Researcher

<sup>‡‡</sup> Senior Researcher

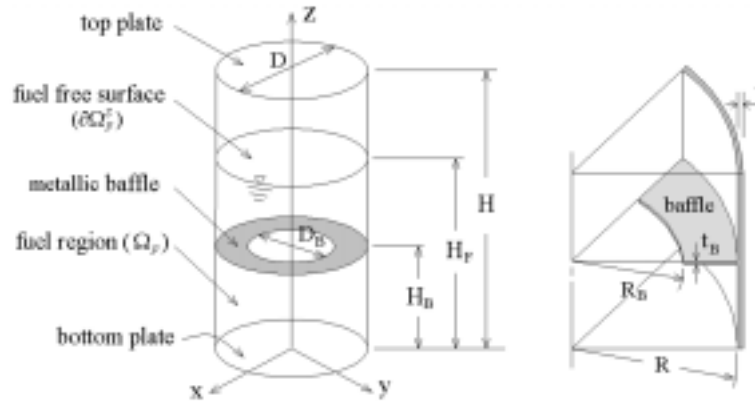


Fig. 1 Cylindrical baffled fuel-storage container with geometry parameters

analysis techniques, such that the profound characteristic analysis was not fully possible.

In the studies of the dynamic response and safe structural design, the main purpose has been to suppress the hydrodynamic force, for which various kinds of mechanical devices have been introduced (Miyata *et al.* 1988, Modi and Welt 1992). Among them, the disc-type elastic baffle, illustrated in Fig. 1, has been reported to be most effective for a wide range of applications (Stephens 1966), because it is more practical and easy to install to the container structure. Hence, the structural stability of moving fuel containers depends definitely on the suitable baffle design. However, needless to say, several design parameters, such as the baffle position and inner hole size, the baffle number and spacing, are inherently associated with the suitable baffle design. As a result, the dynamic analysis of baffled fuel-storage containers has become a more complicated task, owing to the geometric complexity, when compared to that for simple containers without baffle.

However, in order for the successful baffle design the reliable parametric investigation on the structural dynamic characteristics of baffled fuel-storage containers is essential. Fortunately, thanks to the advances in computational analysis techniques such a task could be sufficiently accomplished. In particular, the ALE (arbitrary Lagrangian-Eulerian) numerical method can successfully treat the fluid-structure interaction problems with the moving boundary (Noh *et al.* 1964, Hirt *et al.* 1974), while keeping fairly regular meshes. As will be described later in details, this method combines effectively the Lagrangian and Eulerian methods by introducing the referential domain (or mesh domain) moving arbitrarily.

This paper, as a series of our recent works (Cho *et al.* 2001), aims at the parametric transient analysis of cylindrical baffled fuel-storage tanks, subject to an abrupt vertical acceleration, by utilizing the ALE numerical approach. In fact, a liquid fuel-storage container experiences the extremely high hydrodynamic force, at its boosting stage, so that its transient dynamic response is strongly influenced by the baffle parameters. In this paper, we consider the baffle position and the inner-hole size allowing the fuel flow as the analysis parameters. Through the parametric experiments, we intensively examine the parametric effects of these parameters on the transient dynamic response of the baffled fuel-storage tanks.

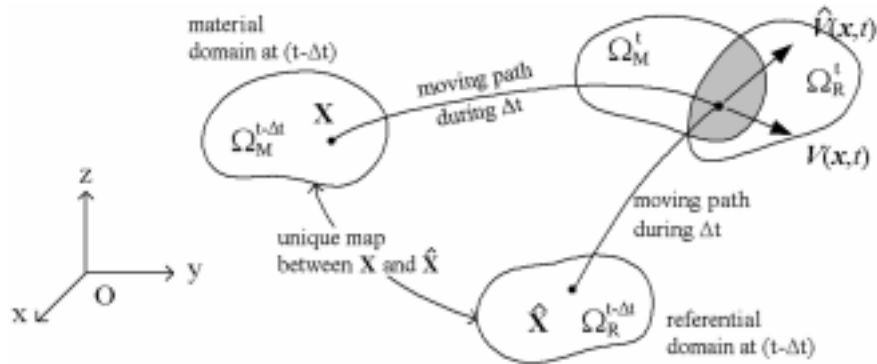


Fig. 2 Relationship between material, referential and spatial domains

## 2. ALE description for fluid flow

Generally, the numerical analysis of unsteady fluid flow has employed the Eulerian or Lagrangian descriptions of motion. In the Eulerian formulation, a referential (or mesh) coordinate is fixed in the space and the fluid moves through elements. By using this method, the analysis of fluid undergoing great distortions can be accomplished with relatively ease and accuracy. But its major disadvantages are the lack of the exact identification of interfaces and the difficulty in tracking the moving boundary. So, it requires any special technique for dealing with the moving interface or boundary, which is usually complicated and may lead to the numerical inaccuracy.

On the other hand, the mesh coordinate in the Lagrangian formulation moves exactly with the fluid particles, so that each element contains the same fluid particles along the flow. As a result, it can precisely identify and track the moving boundary and interface, but it causes the crucial numerical instability owing to the extreme mesh distortion, unless any suitable mesh regulating process is accompanied.

In order to achieve the advantages only in both conventional Eulerian and Lagrangian approaches, the ALE (arbitrary Lagrangian-Eulerian) method, the most effective and robust one for the unsteady flow analysis, has been introduced. Originally, it was initiated by Noh (1964), Hirt *et al.* (1974) for the finite difference scheme. In finite element community, Belytschko *et al.* (1978, 1981 and 1986), Hughes *et al.* (1981, 1982 and 1992) and Kawahara *et al.* (1987) have subsequently adopted the ALE method for the fluid-structure interaction problems. As well, Benson (1989, 1992) and Donea (1982) also made remarkable contribution to this area. Since the ALE method precisely identifies and tracks the moving boundary and interface, while maintaining fairly regular meshes, it can successfully and effectively simulate fluid flow with the moving boundary, free surface flow, large deformation problems, and so on. As will be presented later, this formulation is always accompanied with any kind of remeshing schemes (Winslow 1990, Souli *et al.* 2000) maintaining regular meshes along the fluid flow, in order to prevent the critical time step from being too small.

Referring to Fig. 2, the ALE method is characterized by the arbitrary movement of a reference domain, which is introduced as a third domain additionally to the common material and spatial domains. The material or Lagrangian coordinate  $X$  identifies a material particle  $P$  in the undeformed configuration  $R_0$  at time  $t=0$ . In the deformed configuration  $R_t$ , at time  $t$ , the particle originated at  $P$  moves to the current point  $p$  with the position vector  $x$ . Here,  $x$  is the spatial coordinate

describing the current position of the material particle identified by  $\mathbf{X}$  in the material domain. Differing from the spatial and material coordinates, a referential coordinate  $\hat{\mathbf{X}}$  refers to the computational mesh domain in most cases. Of course, the motion of a continuum can also be described by the referential coordinate.

Naturally, a function  $f$  describing any physical quantity associated with the fluid flow, which is continuous in space and time, can be defined as a function of either  $\mathbf{x}$ ,  $\mathbf{X}$ , or  $\hat{\mathbf{X}}$ . As a result, three types of time derivatives could also be defined as follows:

Material time derivative	Spatial time derivative	Referential time derivative
$\dot{f} = \left. \frac{\partial f(\mathbf{X}, t)}{\partial t} \right _{\mathbf{x}}$	$\frac{\partial f}{\partial t} = \left. \frac{\partial f(\mathbf{x}, t)}{\partial t} \right _{\mathbf{x}}$	$\overset{\circ}{f} = \left. \frac{\partial f(\hat{\mathbf{X}}, t)}{\partial t} \right _{\hat{\mathbf{x}}}$

When we denote  $\mathbf{x}$  and  $\hat{\mathbf{x}}$  be the current spatial position vectors of a material particle and the moving reference coordinate, respectively, measured from the fixed Cartesian coordinate system. Then, the material velocity  $\mathbf{v}$  and the referential velocity  $\hat{\mathbf{v}}$  are defined respectively by

$$\mathbf{v} = \dot{\mathbf{x}} = \left. \frac{\partial \mathbf{x}(\mathbf{X}, t)}{\partial t} \right|_{\mathbf{x}}, \quad \hat{\mathbf{v}} = \dot{\hat{\mathbf{x}}} = \left. \frac{\partial \hat{\mathbf{x}}(\hat{\mathbf{X}}, t)}{\partial t} \right|_{\hat{\mathbf{x}}} \quad (1)$$

For the purpose of ALE representation, one can easily derive the fundamental relationship (Souli *et al.* 2000) between material and referential time derivatives given by

$$\left. \frac{\partial f(\mathbf{X}, t)}{\partial t} \right|_{\mathbf{x}} = \left. \frac{\partial f(\hat{\mathbf{X}}, t)}{\partial t} \right|_{\hat{\mathbf{x}}} + \mathbf{c} \cdot \frac{\partial f}{\partial \mathbf{x}} \quad (2)$$

in which  $\mathbf{c}$  is the relative or convective velocity between the material velocity  $\mathbf{v}$  and the referential velocity  $\hat{\mathbf{v}}$ :

$$\mathbf{c} = \mathbf{v} - \hat{\mathbf{v}} \quad (3)$$

The last term in the right hand side means the convective effect due to the relative motion between the material and referential coordinates.

In the ALE description, the velocity field of referential domain can be arbitrarily chosen, so that the conventional Eulerian or Lagrangian formulations can also be identified:

- $\hat{\mathbf{v}} = 0$  : the referential domain is fixed in space, and which corresponds to the Eulerian viewpoint described in terms of spatial coordinate,
- $\hat{\mathbf{v}} = \mathbf{v}$  : the referential domain moves in space with the same velocity as the particles, and which corresponds to the Lagrangian viewpoint,
- $\hat{\mathbf{v}} \neq \mathbf{v} \neq 0$  : the referential domain moves in space at an arbitrary velocity, and which is general arbitrary Lagrangian-Eulerian viewpoint.

### 3. Incompressible Newtonian flow within the elastic container

The dynamic motion of a structural container occupying the spatial domain  $\Omega$ , in the Cartesian coordinate system, is governed by

$$\sigma_{ij}(\mathbf{u})_{,j} - c\dot{u}_i = \rho(\ddot{u}_i - f_i), \text{ in } \Omega \times [0, T] \quad (4)$$

with initial and boundary conditions:

$$u_i(x_i, 0) = \dot{u}_i(x_i, 0) = 0 \text{ in } \Omega \quad (5)$$

$$u_i = \bar{u}_i, \text{ on } \partial\Omega_D \times [0, T] \quad (6)$$

$$\sigma_{ij}n_j = \bar{t}_i, \text{ on } \partial\Omega_I \times [0, T] \quad (7)$$

In which  $c$ ,  $\rho$  and  $f_i$  are the damping coefficient, the structure density and gravity acceleration components, respectively. The boundary with the outward unit normal vector  $\mathbf{n}$  is composed of the displacement boundary region  $\partial\Omega_D$  and the fluid-structure interface  $\partial\Omega_I$ .

Furthermore, strain-displacement relations and constitutive relations between Cauchy strains and stresses are defined by

$$\varepsilon_{ij} = (u_{i,j} + u_{j,i})/2 \quad (8)$$

$$\sigma_{ij} = 2\mu\varepsilon_{ij} + \lambda\varepsilon_{kk}\delta_{ij} \quad (9)$$

where  $\mu$  and  $\lambda$  are Lamé constants of linear elastic isotropic materials.

On the other hand, the governing equations for the incompressible Newtonian fluid flow, in the ALE description, are obtained by substituting the convection velocity in the Eulerian formulation with the relative convective velocity  $\mathbf{c} = \mathbf{v} - \hat{\mathbf{v}}$  defined in Section 2. Then, the resulting governing equations, composed of the momentum and continuity equations, are as follows:

$$\frac{\partial v_i}{\partial t} + c_j v_{i,j} = \frac{1}{\rho_F} \sigma_{ij,j} + f_i, \text{ in } \Omega_F \times [0, T] \quad (10)$$

$$v_{i,i} = 0, \text{ in } \Omega_F \times [0, T] \quad (11)$$

where  $\rho_F$  denotes the fluid density. The total stress tensor  $\sigma_{ij}$  are given by

$$\sigma_{ij} = -p\delta_{ij} + \mu(v_{i,j} + v_{j,i}) \quad (12)$$

where  $p$  is the pressure, and  $\mu$  is the viscosity coefficient.

The boundary  $\partial\Omega_F$  consists of two kinds of boundary regions, the free surface boundary  $\partial\Omega_F^S$  and the fluid-structure interface  $\partial\Omega_I$ . And the corresponding conditions for velocity  $v_i$  and surface traction  $t_i$  are

$$v_i = \bar{v}_i, \text{ on } \partial\Omega_I \times [0, T] \quad (13)$$

$$\{-p\delta_{ij} + \mu(v_{i,j} + v_{j,i})\}n_j = \bar{t}_i, \text{ on } \partial\Omega_F^S \times [0, T] \quad (14)$$

The surface traction, due mostly to the surface tension, is usually negligible. The initial conditions for velocity and pressure are specified as follows:

$$v_i(x_i, 0) = 0 \quad (15)$$

$$p(x_i, 0) = 0 \quad (16)$$

#### 4. Numerical implementation of the ALE flow equations

One of the major difficulties in the time integration of the ALE Navier-Stokes equations is caused by the presence of the relative convective term that stems from the relative motion between the material and referential frames. Basically, there exist two ways to implement the ALE equations according to conventional two approaches taken in the Eulerian fluid mechanics. The first approach is to solve the fully coupled equations. Hughes *et al.* (1981) and Belytschko *et al.* (1981) adopted this approach for the fluid-structure interaction problem.

The alternative approach is the operator split method, adopted in this paper, in which the time integration at each time step is divided into two phases. First, the Lagrangian phase is performed, in which the mesh moves exactly with the material. Next, through the Eulerian phase, the solutions obtained at the first phase are corrected by taking into account the relative mesh velocity. This method breaks a complex problem into simpler one, and any kind of existing algorithms can be applied, so that it is less expensive and more robust than the fully coupled method. Donea (1982), Kawahara *et al.* (1987), and Benson (1989, 1992) adopted this method.

On the other hand, the mesh (referential domain) velocity field should be specified. Regardless of the term *arbitrary*, it should satisfy the no penetration/slip condition along the fluid-structure interface and the no change in the total fluid volume. In fact, the mesh velocity is determined in the remeshing and smoothing process because the final mesh configuration at the end of each time stage is completed after this process. Needless to say, the smoothing process, a major feather of the ALE method, is to prevent the critical time-step size from being too small.

##### 4.1 Two-phase Lagrangian-Eulerian time integration

In the Lagrangian phase, the relative convective term is dropped out from the ALE Navier-Stokes Eq. (10), so that the mesh domain moves exactly with the material. And, the momentum and continuity Eqs. (10) and (11) are discretized according to the purely explicit Euler time integration method (Zienkiewicz and Taylor 1991). We now summarize the Lagrangian phase.

First, the intermediate velocity  $\tilde{v}_i^L$  is computed from the discretized momentum equation without the pressure and convection terms,

$$\frac{\tilde{v}_i^L - v_i^n}{\Delta t} = \frac{\mu}{\rho_F} (v_{i,j}^n + v_{j,i}^n)_{,j} + f_i \quad (17)$$

$$\tilde{v}_i^L = \bar{v}_i, \quad \text{on } \partial\Omega_t \quad (18)$$

We note here that  $\tilde{v}_i^L$  does not satisfy the continuity constraint.

After that, the final Lagrangian velocity  $v_i^L$  satisfying the continuity condition can be computed by taking into account the pressure  $p^L$  satisfying the incompressibility equation, together with the boundary condition (18)

$$\frac{v_i^L - \tilde{v}_i^L}{\Delta t} = -\frac{1}{\rho_F} p_{,i}^L \quad (19)$$

where the pressure  $p^L$  is determined using

$$p_{,ii}^L = \frac{\rho_F \tilde{v}_{i,i}^L}{\Delta t} \quad (20)$$

This pressure equation is obtained by taking divergence on Eq. (19), together with the incompressibility requirement ( $v_{i,i}^L = 0$ ). For which the next boundary conditions are specified (see Appendix A for Eq. (22)):

$$p^L = 0, \quad \text{on } \partial\Omega_F^S \tag{21}$$

$$p_{,i}^L n_i = 0, \quad \text{on } \partial\Omega_I \tag{22}$$

Once the pressure is determined, the final Lagrangian velocity  $v_i^L$  is determined from Eq. (19), and this process is repeated until the final velocity  $v_i^L$  meets sufficiently the continuity constraint. After this iteration is completed, the current mesh coordinates are updated through

$$x_i^L = x_i^n + \Delta t \cdot v_i^L \tag{23}$$

where superscript  $n$  refers to the previous time stage. If only a Lagrangian calculation is decided to be sufficient the time integration at time stage  $n$  is terminated, otherwise the next Eulerian phase, together with the mesh smoothing, should be followed.

Before we proceed the Eulerian phase, we smooth the distorted mesh caused by the Lagrangian mesh movement, then we have the final mesh coordinates  $x_i^E$ . Then, the mesh velocity  $\hat{v}_i^n$  is automatically determined through

$$\hat{v}_i^n = v_i^L + (x_i^E - x_i^L) / \Delta t \tag{24}$$

Next, the previous Lagrangian-phase velocity  $v_i^L$  and pressure  $p^L$  are corrected by reflecting the relative convective term. Similar to the Lagrangian phase, the intermediate velocity  $\tilde{v}_i^{n+1}$  is first calculated according to

$$\frac{\tilde{v}_i^{n+1} - v_i^L}{\Delta t} + c_j^n v_{i,j}^n = 0, \quad \text{on } c_j^n = (v_i^n - \hat{v}_i^n) \tag{25}$$

$$\tilde{v}_i^{n+1} = \bar{v}_i, \quad \text{on } \partial\Omega_I \tag{26}$$

Of course this intermediate velocity does not satisfy the continuity condition, therefore the correction iteration is employed, as in the Lagrangian phase. The iterative correction is accomplished according to

$$p_{,ii}^{n+1} = \frac{\rho_F \tilde{v}_{i,i}^{n+1}}{\Delta t} \tag{27}$$

$$\frac{v_i^{n+1} - \tilde{v}_i^{n+1}}{\Delta t} = -\frac{1}{\rho_F} p_{,i}^{n+1} \tag{28}$$

in which, the previous essential and natural boundary conditions (18), (21) and (22) are enforced.

#### 4.2 Remeshing and smoothing process

As can be inferred from the previous section, the remeshing process is performed in the Lagrangian phase, while the smoothing process in the Eulerian phase. Therefore, the remeshing process can not be omitted in the two-phase Lagrangian-Eulerian method. But, reminding that the smoothing is to prevent the critical time-step size from being too small, the necessity of the Eulerian phase is of course judged based on the mesh distortion intensity against the allowable critical time-

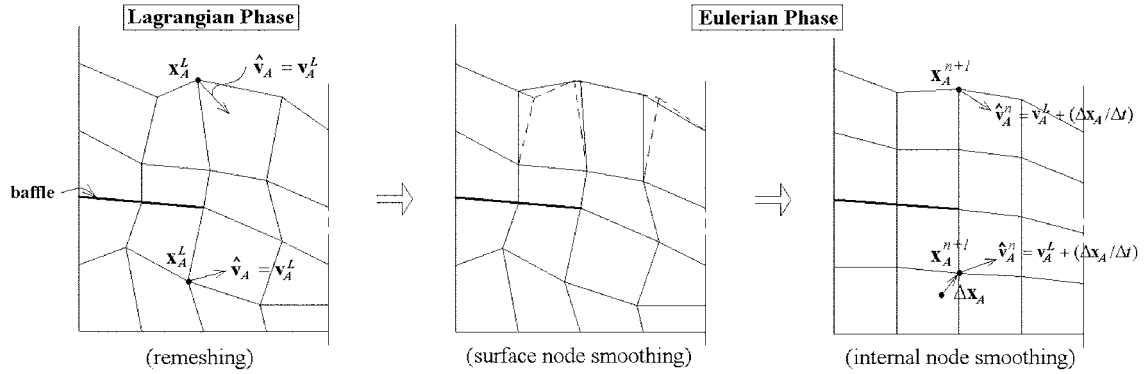


Fig. 3 Remeshing and smoothing process in the two-phase Lagrangian-Eulerian approach

step size. As a result, the decision policy of the smoothing process is naturally problem- and analyst-dependent (Souli *et al.* 2000).

Fig. 3 illustrates the two-dimensional remeshing and smoothing process composed of three steps, which is used in our study, by employing the simple averaging methods (Souli *et al.* 2000). According to the simple averaging algorithm, any node  $A$  (except for the fluid-structure interface nodes) is iteratively smoothed by

$$\mathbf{x}_A^{n+1} = \mathbf{x}_A^L + \frac{1}{M_A} \sum_{k=1}^{M_A} \mathbf{x}_k \quad (29)$$

where  $M_A$  is the number of surrounding nodes of node  $A$  to be smoothed. In this process, remeshing is firstly performed at the end of the Lagrangian phase, after that the smoothing process is followed. Usually, the smoothing is separately performed such that the free-surface nodes are firstly smoothed, and next the interior nodes are smoothed.

It is worthy noting that the remeshing and smoothing process satisfies essentially the no penetration/slip condition along the fluid-structure interface and the no change in total fluid volume. Needless to say, it is because the velocity fields at both phases are determined while satisfying the boundary and continuity conditions, as mentioned in the previous section.

## 5. Coupled fluid-structure finite element analysis

### 5.1 Finite element approximations

Applying usual variational formulation and the isoparametric finite element approximation to the structural dynamic Eq. (4), we have

$$\mathbf{M}\ddot{\mathbf{u}} + \mathbf{C}\dot{\mathbf{u}} + \mathbf{K}\mathbf{u} = \mathbf{F} \quad (30)$$

In which,  $\mathbf{F}$  the load vector due to the self weight and the hydrodynamic pressure given by

$$\mathbf{F} = \int_{\Omega} \Phi^T(\rho \mathbf{f}) dv + \int_{\partial\Omega_f} \Phi^T \mathbf{p} ds \quad (31)$$

where  $\Phi$  indicates the  $(3 \times 3N)$  matrix composed of  $N$  basis functions, and  $\mathbf{p}$  the hydrodynamic pressure force in Cartesian coordinates. For our undamped storage container, we can rewrite Eq. (30) in a time discretized form, together with the mass-matrix diagonalization

$$\ddot{\mathbf{u}}^n = \mathbf{M}^{-1}(\mathbf{F}^n - \mathbf{K}\mathbf{u}^n) \quad (32)$$

When we employ the explicit central difference scheme, time-step-wise accelerations are computed from Eq. (31), and time-step-wise velocities and displacements are determined through

$$\dot{\mathbf{u}}^{n+1/2} = \dot{\mathbf{u}}^{n-1/2} + \ddot{\mathbf{u}} \cdot (\Delta t^{n-1} + \Delta t^n)/2 \quad (33)$$

$$\mathbf{u}^{n+1} = \mathbf{u}^n + \dot{\mathbf{u}}^{n+1/2} \cdot \Delta t^n \quad (34)$$

In addition, the structure configuration is updated by adding the current displacement to the initial configuration such that

$$\mathbf{x}^{n+1} = \mathbf{x}^0 + \mathbf{u}^{n+1} \quad (35)$$

On the other hand, the critical time-step size  $(\Delta t)_{crit}$  for the numerical convergence and stability is determined by the CFL condition (Cook *et al.* 1989):

$$(\Delta t)_{crit} = h/s \quad (36)$$

where  $h$  is the smallest distance between two adjacent nodes, and  $s$  the speed of sound in structure.

Next, for the spatial approximation of the ALE Navier-Stokes equations, we apply the variational principle to the previous six time-discretized equations, Eqs. (17), (19)-(20) in the Lagrangian phase and Eqs. (25), (27)-(28) in the Eulerian phase. After that we approximate the fuel velocity and pressure such that

$$\mathbf{v}^h = \Phi \mathbf{v}, \quad \mathbf{c}^h = \Phi \mathbf{c}, \quad p^h = \Psi \mathbf{p} \quad (37)$$

with the basis function matrix  $\Phi$  used in Eq. (31) and the  $(1 \times N)$  basis function matrix. Introducing these approximate forms into the variational forms, we have three matrix equations for the Lagrangian phase

$$\mathbf{H}^L \tilde{\mathbf{v}}^L = \mathbf{H}^n \mathbf{v}^n - (\Delta t)(\mathbf{S}^n \mathbf{v}^n - \mathbf{R}_v^n) \quad (38a)$$

$$\mathbf{G}^L \mathbf{p}^L = -\rho_F (\Delta t)^{-1} \mathbf{Q}^L \tilde{\mathbf{v}}^L - \mathbf{R}_p^L \quad (38b)$$

$$\mathbf{H}^L \mathbf{v}^L = \mathbf{H}^L \tilde{\mathbf{v}}^L - (\Delta t) \rho_F^{-1} \mathbf{Q}^L \mathbf{p}^L \quad (38c)$$

and three for the Eulerian phase

$$\mathbf{H}^{n+1} \tilde{\mathbf{v}}^{n+1} = \mathbf{H}^L \mathbf{v}^L - (\Delta t) \mathbf{A}^n \mathbf{v}^n \quad (39a)$$

$$\mathbf{G}^{n+1} \mathbf{p}^{n+1} = -\rho_F (\Delta t)^{-1} \mathbf{Q}^{n+1} \tilde{\mathbf{v}}^{n+1} - \mathbf{R}_p^{n+1} \quad (39b)$$

$$\mathbf{H}^{n+1} \mathbf{v}^{n+1} = \mathbf{H}^{n+1} \tilde{\mathbf{v}}^{n+1} - (\Delta t) \rho_F^{-1} \mathbf{Q}^{n+1} \mathbf{p}^{n+1} \quad (39c)$$

in which superscripts  $n$ ,  $L$  and  $n+1$  of matrices indicate that corresponding matrices are integrated over the mesh domains and values at time stages  $n$ ,  $L$  (Lagrangian phase) and  $(n+1)$  (Eulerian phase), respectively. The detailed definition of above matrices is given in Appendix B.

As is well known, the critical time-step size  $(\Delta t)_{crit}$  for the explicit flow analysis is determined according to the Courant criterion (Cook *et al.* 1989):

$$(\Delta t)_{crit} = h/(s + v) \quad (40)$$

when the flow velocity  $v$  is near or over Mach number. By comparing with one in Eq. (36) for the explicit structural dynamic analysis, we realize that the critical time-step size for the coupled fluid-structure analysis becomes one for the flow analysis, provided both mesh sizes are almost equal.

## 5.2 Coupled time-incremental FEM analysis

As described earlier, the structure deformation and the hydrodynamic pressure interact along the common fluid-structure interface  $\partial\Omega_f$ . In order to solve the coupled time-history responses, we use the time-incremental numerical scheme. According to this iterative scheme, we first solve the structure response, after that we perform the two-phase Lagrangian-Eulerian flow analysis. The overall numerical procedure is summarized as follows.

Step 1: structure analysis ; With  $\mathbf{p}^n$ ,  $\mathbf{u}^n$  and  $\dot{\mathbf{u}}^{n-1/2}$  obtained from the previous time stage, we compute  $\ddot{\mathbf{u}}^n$  from Eq. (32), and  $\dot{\mathbf{u}}^{n+1/2}$  and  $\mathbf{u}^{n+1}$  using Eqs. (33) and (34). (For the initial time stage (i.e.,  $n=0$ ),  $\ddot{\mathbf{u}}^0$  is computed with initial conditions  $\mathbf{p}^0 = \mathbf{u}^0 = 0$ , and furthermore  $\dot{\mathbf{u}}^{1/2}$  with initial velocity condition  $\dot{\mathbf{u}}^{-1/2} = \dot{\mathbf{u}}^0 = 0$ .) With the computed displacement  $\mathbf{u}^{n+1}$ , we update the structure mesh according to Eq. (35).

Step 2: Lagrangian-phase flow analysis ; According to Eq. (38a) we first compute the intermediate velocity  $\tilde{\mathbf{v}}^L$  with  $\mathbf{v}^n$  from the previous time stage and the boundary condition  $\bar{\mathbf{v}} = (\mathbf{u}^{n+1} - \mathbf{u}^n)/\Delta t$ . (Of course, the initial velocity condition  $\mathbf{v}^0 = 0$  is used for the initial time stage.) After that, we iteratively solve Eqs. (38b) and (38c) by enforcing the same velocity boundary condition and the pressure boundary conditions (21) and (22), in order for the Lagrangian velocity  $\mathbf{v}^L$ . We next perform the remeshing process for the fluid domain according to Eq. (23). If  $t \geq T$  we terminate the time iteration loop, otherwise we calculate the critical time step. When judged as  $(\Delta t)_{crit} < (\Delta t)_{pre}$  we go to Step 3, otherwise we go to Step 1. In which  $(\Delta t)_{pre}$  indicates the allowable time-step size preset by the analyst at the beginning.

Step 3: Eulerian-phase flow analysis ; According to Eq. (24) we first calculate the mesh velocity  $\hat{\mathbf{v}}^n$ , and then compute the intermediate velocity  $\tilde{\mathbf{v}}^{n+1}$  using Eq. (39a). Next, we iteratively solve Eqs. (39b) and (39c) for calculating the final flow velocity  $\mathbf{v}^{n+1}$  and hydrodynamic pressure  $\mathbf{p}^{n+1}$ . The enforcement of velocity and pressure boundary conditions are same as in Step 2. After the Eulerian phase is completed, we go to Step 1, for the next iteration when  $t < T$ , otherwise we terminate the time iteration loop.

## 6. Numerical experiments

### 6.1 Description of the model problem

Fig. 4(a) shows a model fuel-storage tank, with a baffle of the same material for the container, in which liquid fuel is filled up 90% of the total container-volume (i.e.,  $H_L = 0.9 H$ ). The container is moving in the  $z$ -direction with constant vertical acceleration 10 g, against the gravitational force,

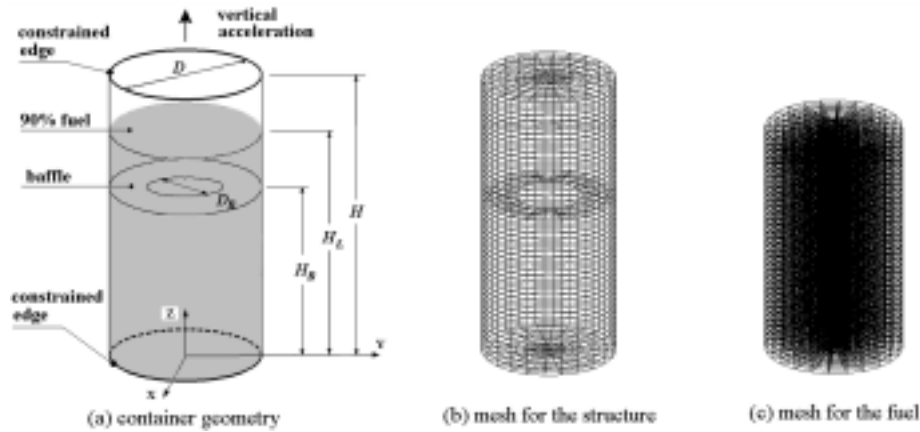


Fig. 4 Cylindrical fuel-storage container with a baffle and its FEM meshes

Table 1 Material data taken for numerical experiments

Fluid		Structure	
Density, $\rho$	$8.15 \times 10^2 \text{ kg/m}^3$	Density, $\rho$	$2.78 \times 10^3 \text{ kg/m}^3$
Viscosity coefficient, $\mu$	$8.15 \times 10^{-4} \text{ kg/m} \cdot \text{s}$	Young's modulus, $E$	$7.24 \times 10^{10} \text{ N/m}^2$
Bulk modulus, $\kappa$	$2.2 \times 10^9 \text{ N/m}^2$	Poisson's ratio, $\nu$	0.33

which applies along two edges of the top and bottom plates. This external loading is implemented numerically by specifying the time-stage-wise displacement boundary condition along the edges. Material data are contained in Table 1. And geometry dimensions are as follows:  $D = 0.4 \text{ m}$ ,  $H = 1.0 \text{ m}$ ,  $t = 2.54 \text{ mm}$  and  $t_B = 3.0 \text{ mm}$ , respectively. In accordance with the objective of this paper, the baffle location  $H_B$  and the inner-hole diameter  $D_B$  are taken variable: three cases of  $D_B/D = 1/4$ ,  $1/2$  and  $3/4$ , and six cases of  $H_B/H = 0.1, 0.3, 0.5, 0.7, 0.8$  and  $0.85$ . As a result, total 18 cases are parametrically examined.

Figs. 4(b) and 4(c) show finite element meshes of the structure and the fuel, for which bilinear shell elements and trilinear solid elements are respectively used. Total element numbers are as follows: 1,704 elements for the structure and 9,810 elements for the fuel region. Both meshes have the same mesh partition over the fluid-structure interface  $\partial\Omega_I$ , in order for the easy numerical data communication between two coupled fields. Furthermore, both meshes share common nodes along the interface based upon that the vertical fluid free-surface fluctuation near the interface is not remarkable, differing from the horizontal sloshing motion. The observation time  $T$  is set 0.06 sec, and the speeds of sound  $c$  are 1,643 m/sec in fuel and 5,053 m/sec in structure, respectively. Furthermore the peak flow velocity is 6.27 m/sec from the preliminary experiment. Then, according to Eqs. (36) and (41), we obtained the critical time-step sizes for two initial meshes:  $(\Delta t)_{crit}^{st} = 1.41 \times 10^{-6} \text{ sec}$  and  $(\Delta t)_{crit}^{fl} = 4.26 \times 10^{-6} \text{ sec}$ , respectively. Based upon these initial critical values, we set the minimum allowable time step-size  $(\Delta t)_{tol}$ , for our flow analysis, by  $1.4 \times 10^{-6} \text{ sec}$ .

## 6.2 Numerical results to the baffle location and inner-hole size

Referring to Fig. 4, cylindrical fuel-storage tank exhibits the peak dynamic deformation at the

center of the bottom plate, when it accelerates vertically, and its transient dynamic response is crucial within a short initial time period starting from the boosting. On the other hand, the deformation field in any linearly elastic body characterizes the stress field. For this reason, we focus our attention on the relative displacement at the center of the bottom plate during the time period of 60 m/sec. Here, the term *relative* indicates the displacement measured with respect to the constrained edge, and hereafter the displacement is used in the relative sense.

Figs. 5-7 present the parametric time-history responses of the container displacement at the bottom center for 18 cases, where the case without baffle is included in order for a comparison purpose. Above all, we can observe that the baffled cases, except for two cases with  $D_B/D$  of  $3/4$ , produce the relatively smaller displacement than the no baffle case. For the cases where the baffle is installed at relatively lower positions below  $H_B/H = 0.5$ , the time-history responses are quite similar

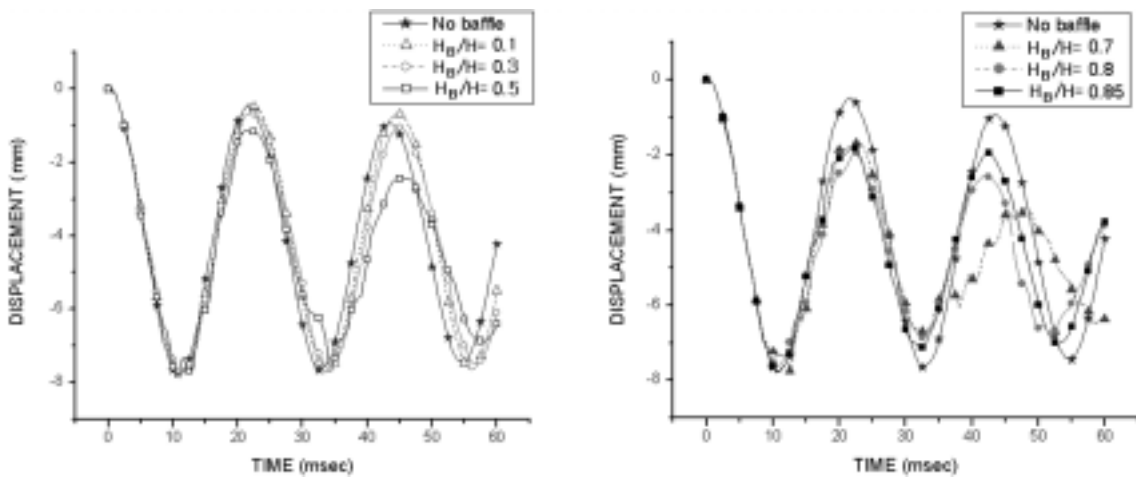


Fig. 5 Time-history responses of the displacement at bottom center ( $D_B/D = 3/4$ )

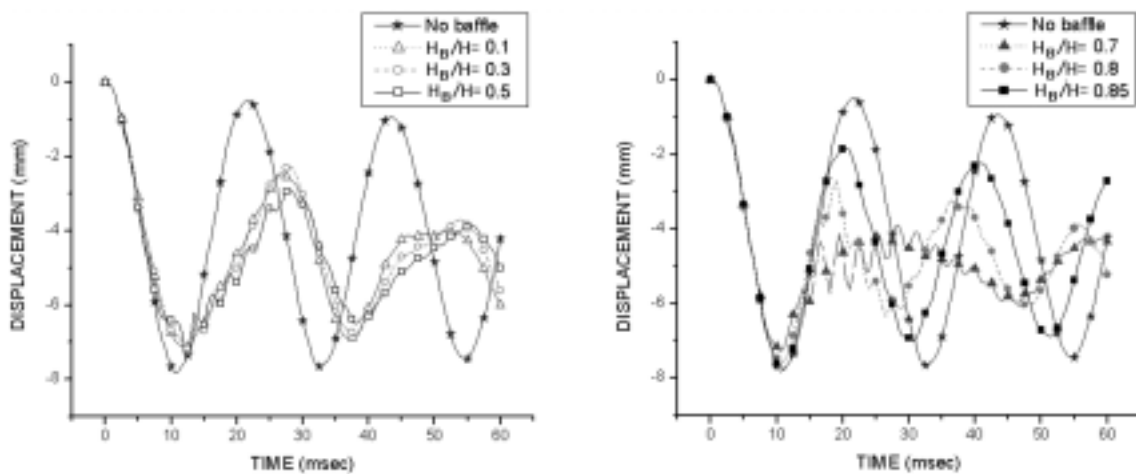


Fig. 6 Time-history responses of the displacement at bottom center ( $D_B/D = 2/4$ )

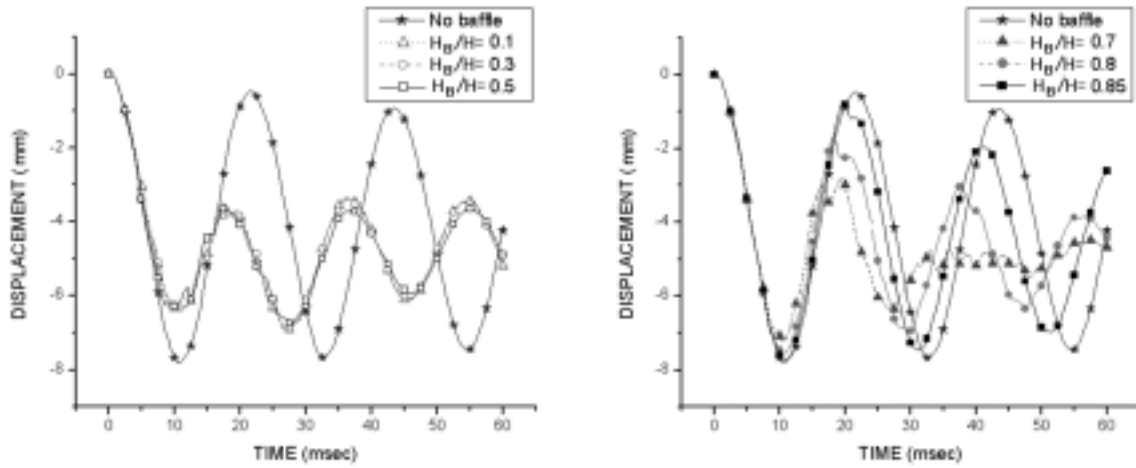


Fig. 7 Time-history responses of the displacement at bottom center ( $D_B/D = 1/4$ )

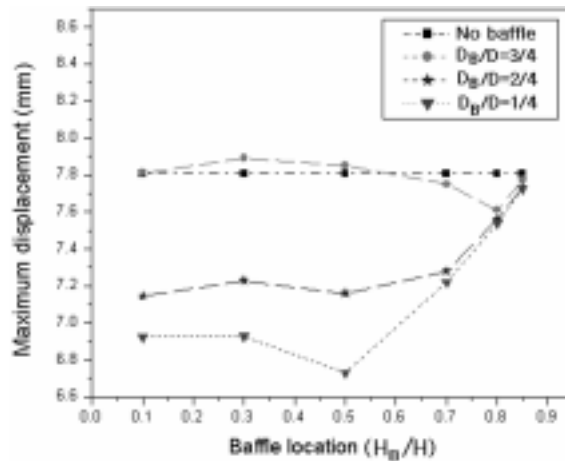


Fig. 8 Comparison of maximum displacement according to  $H_B/H$  and  $D_B/D$

to the baffle location, but their magnitudes decrease as the baffle inner-hole size  $D_B/D$  decreases. While when the baffle is positioned higher above  $H_B/H = 0.5$ , the time-history response is considerably dependent on the baffle location, such that the peak displacement increases together with the baffle location  $H_B/H$  and the response frequency decreases as  $H_B/H$  decreases. In particular, such a trend is remarkable when the baffle inner-hole becomes wider.

Next, we analyze the numerical results from three points of view: the absolute maximum displacement, the response frequency and the logarithmic decrement, as shown in Figs. 8-10. Here, the logarithmic decrement  $\chi_d$  is defined by

$$\chi_d = \frac{\ln(d_1/d_N)}{N} \tag{41}$$

in which and denotes the absolute displacements at the first peak and the available  $N$ th peak in time-history responses.

The absolute maximum displacement, from Fig. 8, decreases in proportion to the decrease of  $D_B/D$ , but this dependence on the baffle inner-hole size approaches the case without baffle. In particular, the case of  $D_B/D = 3/4$ , the difference with the no baffle case is minute. Needless to say, it is because the hydrodynamic force acting on the bottom plate becomes smaller as the baffle inner-hole size decreases by suppressing more the fluid flow. However, the flow suppression becomes negligible as the baffle goes up to the fuel free surface. The variation of maximum displacement to the baffle location, when  $H_B/H \leq 0.5$ , is not shown remarkable, when compared to one with respect to the baffle inner-hole size. The smallest value in maximum displacements is obtained when  $D_B/D = 3/4$  and  $H_B/H = 0.5$ . From this parametric result, we can conclude the baffle effect reduces either the baffle location approaches the free surface or the baffle inner-hole size becomes larger.

Fig. 9 represents the variation of response frequency, and which is for estimating the stabilization tendency in transient dynamic response. In order words, the dynamic response becomes more stable

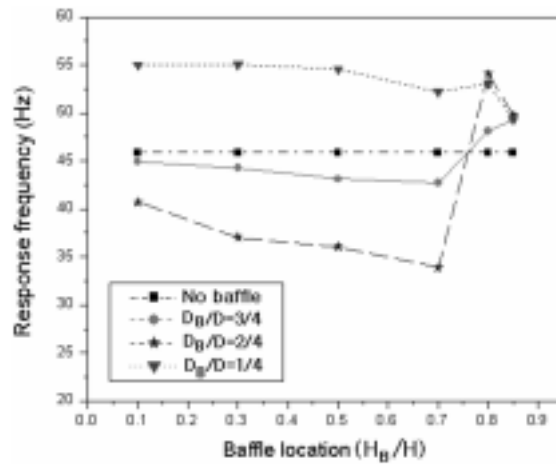


Fig. 9 Comparison of response frequency according to  $H_B/H$  and  $D_B/D$

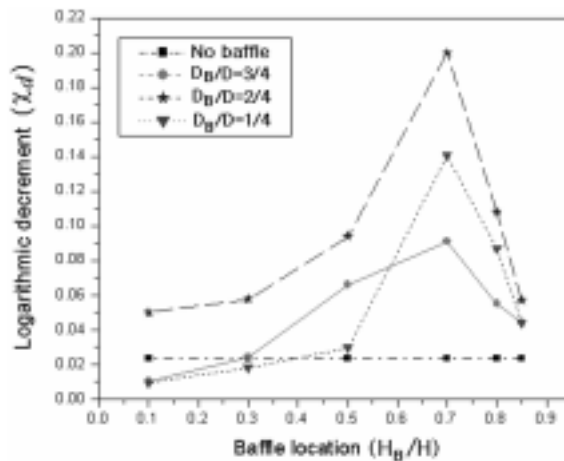


Fig. 10 Comparison of logarithmic decrement according to  $H_B/H$  and  $D_B/D$

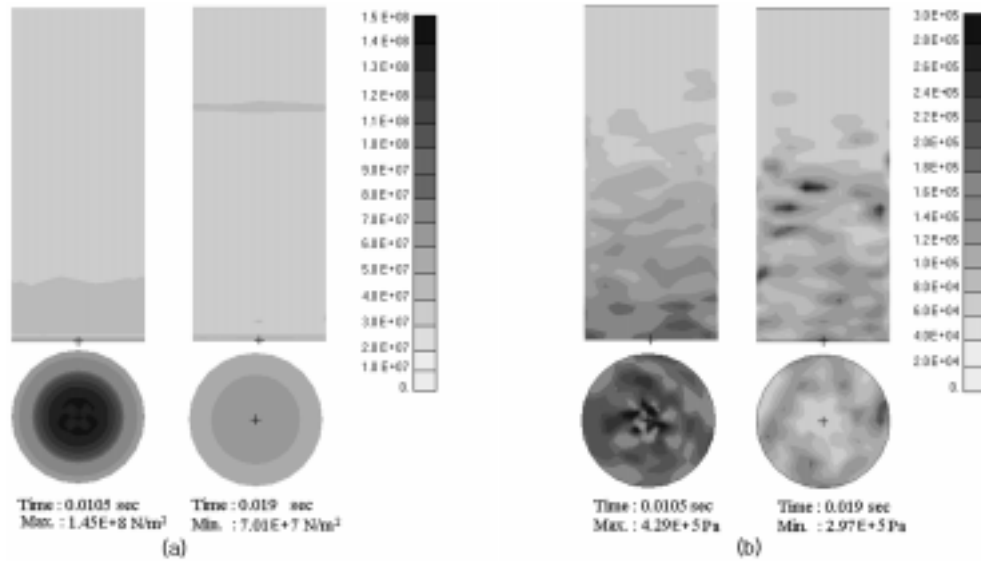


Fig. 11 Distribution patterns at maximum and minimum: (a) stress distributions; and (b) hydrodynamic pressure distributions ( $D_B/D = 2/4$  and  $H_B/H = 0.7$ )

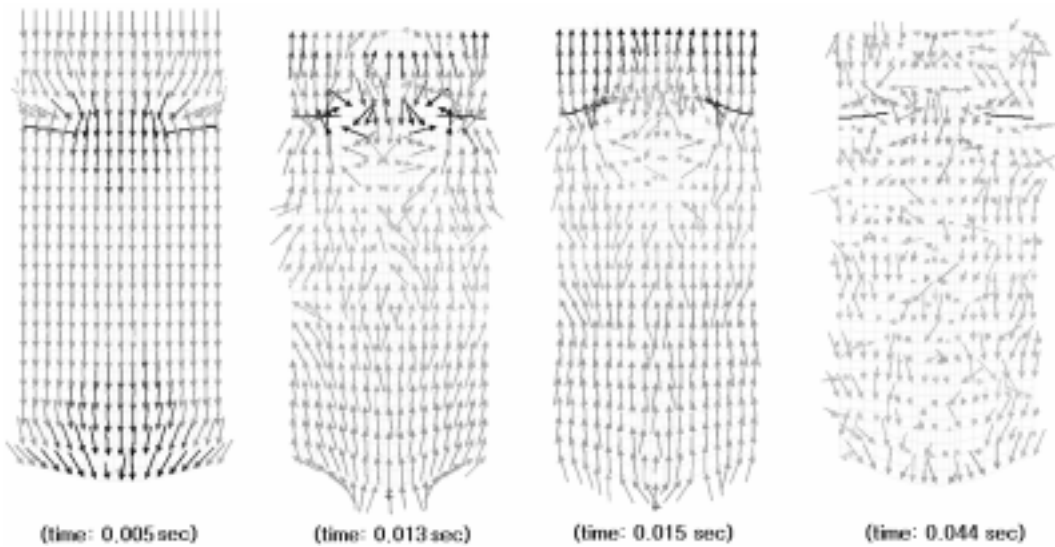


Fig. 12 Flow patterns of interior liquid fuel ( $D_B/D = 2/4$  and  $H_B/H = 0.7$ )

as the response frequency decreases. By comparing with respect to the baffle inner-hole size, the case with  $D_B/D = 1/4$  exhibits the highest frequency while the case with  $D_B/D = 2/4$  the lowest one, but this distinction disappears when the baffle location approaches the fuel free surface. This can be explained as follows. Until the critical  $D_B/D$  the decrease of baffle inner-hole size delays continuously the major fluid flow, but further decrease beyond the critical value separates the major fluid flow into the compartmented flow regions, as can be inferred from the next Fig. 12. In general, the

compartmented liquid container exhibits higher response frequency compared to non-compartmented one (Abramson and Graza 1964). On the other hand, the response frequency decreases, even though slightly, as the baffle location goes up when  $H_B/H \leq 0.7$ , but it remarkably increases to the same limit when  $H_B/H > 0.7$ . Hence, one should determine a suitable baffle inner-hole size by combining this tendency with the previous result. While, the baffle location should not be too high or too low.

The variation of logarithmic decrement is represented in Fig. 10, where we confirm that almost all cases have higher decrements than the no baffle case. Regardless of the baffle inner-hole size, the logarithmic decrement increases with the baffle location until  $H_B/H = 0.7$ , but it strictly drops to the case without baffle when  $H_B/H > 0.7$ . In the same manner, the baffle inner-hole size  $D_B/D$  of  $2/4$  produces the best logarithmic decrement. Considering all of three parametric results, we conclude that the suitable baffle location and inner-hole size, from 18 parametric cases for our model tank, are as follows:  $H_B = 0.7 H$  and  $D_B = 0.5 D$ .

For the baffle case considered most suitable, we trace the time-history response of the structure effective stress along time and represent the effective stress distributions when it reaches maximum and minimum in Fig. 11(a). Where, we see that the maximum stress occurred at the bottom center is almost two times of that in the minimum stress distribution. Corresponding hydrodynamic-pressure distributions at both time stages are given in Fig. 11(b). Flow patterns at four different time stages are also given in Fig. 12. We first realize that the initial simple and uniform flow becomes non-uniform and complex as time goes. In particular, the localized circulating flow around the baffle tip is remarkable.

## 7. Conclusions

In this paper, transient dynamic characteristics of cylindrical fuel-storage container with a baffle, which accelerates abruptly in the vertical direction, were numerically investigated. For this goal, we employed the ALE finite element method for effectively maintaining the fluid mesh to be fairly regular. Furthermore, the ALE Navier-Stokes equations were solved by two-phase Lagrangian-Eulerian scheme, together with the selective mesh-smoothing algorithm by presetting the minimum allowable time-step size. Through the numerical implementation, we confirm that the coupled time-incremental ALE finite element method successfully and effectively treats the baffles moving container.

In order to examine parametrically the baffle effects, we took the baffle location and inner-hole size as the simulation parameters. From the numerical results of eighteen combinations of parameters, we could find out the parametric effects of both parameters on three major dynamic characteristics: the maximum displacement, the response frequency and the logarithmic decrement. As well, we could choose the most suitable combination of the baffle location and inner-hole size.

We believe that the current parametric study can suggest the research direction in the optimal baffle design involving more design parameters for more general situations.

## Acknowledgements

The authors(SYL and JRC) gratefully acknowledge the financial support for this work by Agency for Defense Development under *Contract No. ADD-00-5-6*.

## References

- Abramson, H.N. and Garza, L.R. (1964), "Some measurements of the effects of ring baffles in cylindrical tanks", *J. Spacecraft Rockets*, **1**(5), 560-564.
- Belytschko, T. and Kennedy, J.M. (1978), "Computer models for subassembly simulation", *Nucl. Engrg. Des.*, **49**, 17-38.
- Benson, D.J. (1989), "An efficient, accurate, simple ALE method for nonlinear finite element programs", *Comput. Meths. Appl. Mech. Engrg.*, **72**, 305-350.
- Benson, D.J. (1992), "Computational methods in Lagrangian and Eulerian hydrocodes", *Comput. Methods Appl. Mech. Engrg.*, **99**, 235-394.
- Brooks, A.N. and Hughes, T.J.R. (1982), "Streamline upwind/Petrov-Galerkin formulation for convection dominated flows with particular emphasis on the incompressible Navier-Stokes equations", *Comput. Methods Appl. Mech. Engrg.*, **32**, 199-259.
- Cho, J.R., Song, J.M. and Lee, J.K. (2001), "Finite element techniques for the free-vibration and seismic analysis of liquid-storage tanks", *Finite Elements in Analysis and Design*, **37**(6-7), 467-483.
- Cho, J.R. and Song, J.M. (2001), "Assessment of classical numerical models for the separate fluid-structure modal analysis", *J. Sound and Vib.*, **239**(5), 995-1012.
- Cook, R.D., Malkus, D.S. and Plesha, M.E. (1989), *Concepts and Applications of Finite Element Analysis*, John Wiley & Sons, Singapore.
- Donea, J., Giuliani, S. and Halleux, J.P. (1982), "An arbitrary Lagrangian-Eulerian finite element method for transient dynamic fluid-structure interactions", *Comput. Methods Appl. Mech. Engrg.*, **33**, 689-723.
- Epperson, T.B., Brown, R. and Abramson, H.N. (1961), "Dynamic loads resulting from fuel motion in missile tanks," *Advances in Ballistic Missile and Space Technology*, **II**, 313-327.
- Hirt, C.W., Amsden, A.A. and Cook, J.L. (1974), "An arbitrary Lagrangian-Eulerian computing method for all flow speeds", *J. Comput. Phy.*, **14**, 227-253.
- Hughes, T.J.R., Liu, W.K. and Zimmerman, T.K. (1981), "Lagrangian-Eulerian finite element formulation for incompressible viscous flows", *Comput. Methods Appl. Mech. Engrg.*, **29**, 329-349.
- Kennedy, J.M. and Belytschko, T.B. (1981), "Theory and application of a finite element method for arbitrary Lagrangian-Eulerian fluids and structures", *Nucl. Engrg. Des.*, **68**, 129-146.
- Liu, W.K., Belytschko, T. and Chang, H. (1986), "An arbitrary Lagrangian-Eulerian finite element method for path dependent materials", *Comput. Methods Appl. Mech. Engrg.*, **58**, 227-245.
- Miyata, T., Yamada, H. and Saito, Y. (1988), "Suppression of tower-like structure vibration by damping effect of sloshing water contained", *Transaction of Japan Society of Civil Engineering*, **34A**, 617-626.
- Noh, W.F. (1964), "CEL: a time-dependent, two-space-dimensional, coupled Eulerian-Lagrangian code", *Methods in Computational Physics* (Alder et al. eds.), 117-179.
- Nomura, T. and Hughes, T.J.R. (1992), "An arbitrary Lagrangian-Eulerian finite element method for interaction of fluid and a rigid body", *Comput. Methods Appl. Mech. Engrg.*, **95**, 115-138.
- Ramaswamy, B. and Kawahara, M. (1987), "Arbitrary Lagrangian-Eulerian finite element method for unsteady, convective, incompressible viscous free surface fluid flow", *Int. J. Numer. Methods Fluids*, **7**, 1053-1075.
- Souli, M., Ouahsine, A. and Lewin, L. (2000), "ALE formulation for fluid-structure interaction problems", *Comput. Methods Appl. Mech. Engrg.*, **190**, 659-675.
- Stephens, D.G. (1966), "Flexible baffles for slosh damping", *J. Spacecraft Rockets*, **3**(5), 765-766.
- Welt, F. and Modi, V.J. (1992), "Vibration damping through liquid sloshing, part 2: experimental results", *J. Vib. Acoust.*, **114**, 17-23.
- Winslow, A.M. (1990), "Equipotential zoning of the interior of a three-dimensional mesh", Lawrence Radiation Laboratory, UCRL-7312.
- Zienkiewicz, O.C. and Taylor, R.L. (1991), *The Finite Element Method*, **2**, McGraw-Hill, New York.

## Appendix A: Derivation of the boundary condition Eq. (22)

Taking divergence on Eq. (10) in the Lagrangian phase, together with the relation (12), results in

$$p_{,i} = -\rho_F \left\{ \frac{\partial v_i}{\partial t} - \frac{\mu}{\rho_F} (v_{i,j} + v_{j,i})_{,j} - f_i \right\} \quad (\text{A1})$$

In which the last two terms on the right-hand-side are related to the intermediate velocity through Eq. (17). Meanwhile, we want to compute  $p^L$  which enforces  $v_i^L$  to satisfy the incompressibility condition, so that we would let  $\frac{\partial v_i}{\partial t} = \frac{v_i^L - v_i^n}{\Delta t}$ . Substituting these into Eq. (A1) leads to

$$\begin{aligned} p_{,i}^L &= -\rho_F \left( \frac{v_i^L - v_i^n}{\Delta t} - \frac{\tilde{v}_i^L - v_i^n}{\Delta t} \right) \\ &= -\frac{\rho_F}{\Delta t} (v_i^L - \tilde{v}_i^L) \end{aligned} \quad (\text{A2})$$

From the non-penetration condition along the fluid-structure interface  $\partial\Omega_I$ , we obtain Eq. (22):

$$\nabla p^L \cdot \mathbf{n} = -\frac{\rho_F}{\Delta t} (\mathbf{v}^L - \tilde{\mathbf{v}}^L) \cdot \mathbf{n} = 0, \quad \text{on } \partial\Omega_I \quad (\text{A3})$$

## Appendix B: Definition of matrices used in the flow analysis

For the matrix-operation convenience, we introduce two partial differential operators  $\mathbf{D}_1$  and  $\mathbf{D}_2$

$$\mathbf{D}_1^T = \{ \partial/\partial x, \partial/\partial y, \partial/\partial z \} \quad (\text{B1})$$

$$\mathbf{D}_2^T = 2 \begin{bmatrix} \partial/\partial x & 0 & 0 & \partial/\partial y & 0 & \partial/\partial z \\ 0 & \partial/\partial y & 0 & \partial/\partial x & \partial/\partial z & 0 \\ 0 & 0 & \partial/\partial z & 0 & \partial/\partial y & \partial/\partial x \end{bmatrix} \quad (\text{B2})$$

and, two operators defined by

$$\mathbf{B} = \mathbf{D}_1^T \Phi, \quad \mathbf{L} = \mathbf{D}_2 \Phi \quad (\text{B3})$$

Then, the matrices in Eqs. (38a)-(39c) are defined by

$$\mathbf{H} = \int_{\Omega_f(t)} \Phi^T \Phi dv \quad (\text{B4})$$

$$\mathbf{S} = (\rho_F/2\mu) \int_{\Omega_f(t)} \mathbf{L}^T \mathbf{L} dv \quad (\text{B5})$$

$$\mathbf{R}_V = \int_{\Omega_f(t)} \Phi^T f dv + \int_{\partial\Omega_1(t)} \Phi^T [(\mathbf{n}^T \mathbf{D} \mathbf{I} + (\mathbf{n} \mathbf{D}^T)^T)] \Phi v ds \quad (\text{B6})$$

$$\mathbf{G} = \int_{\Omega_f(t)} (\mathbf{D}_1 \Psi)^T \mathbf{D}_1 \Psi dv \quad (\text{B7})$$

$$\mathbf{Q} = \int_{\Omega_f(t)} \Psi^T \mathbf{B} dv \quad (\text{B8})$$

$$\mathbf{R}_P = \int_{\partial\Omega_1(t)} \Psi^T (\partial p / \partial n) ds \quad (\text{B9})$$

$$\mathbf{A} = \int_{\Omega_f(t)} \Phi^T (\mathbf{c}^T \mathbf{B}^T \mathbf{I}) \Phi dv \quad (\text{B10})$$

where,  $\mathbf{n} = \{n_x, n_y, n_z\}^T$  and,  $\mathbf{I}$  the  $(3 \times 3)$  identity matrix.